A&A 669, A115 (2023)
https://doi.org/10.1051/0004-6361/202244959

Astronomy & Astrophysics

Ca triplet metallicities and velocities for 12 globular clusters toward the galactic bulge⋆

D. Geisler[1,2,3], M. C. Parisi[4,5], B. Dias[6], S. Villanova[1], F. Mauro[7], I. Saviane[8], R. E. Cohen[9], C. Moni Bidin[7], and D. Minniti[10,11]

[1] Departmento de Astronomía, Universidad de Concepción, Casilla 160-C Concepción, Chile
[2] Departamento de Física y Astronomía, Universidad de La Serena, Avenida Juan Cisternas 1200, La Serena, Chile
[3] Instituto de Investigación Multidisciplinario en Ciencia y Tecnología, Universidad de La Serena Benavente 980, La Serena, Chile
e-mail: dgeisler@astroudec.cl
[4] Observatorio Astronómico, Universidad Nacional de Córdoba, Laprida 854, X5000BGR Córdoba, Argentina
e-mail: cparisi@unc.edu.ar
[5] Instituto de Astronomía Teórica y Experimental (CONICET-UNC), Laprida 854, X5000BGR Córdoba, Argentina
[6] Instituto de Alta Investigación, Sede Esmeralda, Universidad de Tarapacá, Av. Luis Emilio Recabarren 2477, Iquique, Chile
[7] Instituto de Astronomía, Universidad Católica del Norte, Av. Angamos 0610, Antofagasta, Chile
[8] European Southern Observatory, Casilla 19001, Santiago, Chile
[9] Department of Physics and Astronomy, Rutgers the State University of New Jersey, 136 Frelinghuysen Road., Piscataway, NJ 08854, USA
[10] Instituto de Astrofísica, Facultad de Ciencias Exactas, Universidad Andrés Bello, Av. Fernández Concha 700, Las Condes, Santiago, Chile
[11] Vatican Observatory, V00120 Vatican City State, Italy

Received 12 September 2022 / Accepted 4 October 2022

ABSTRACT

Context. Globular clusters (GCs) are excellent tracers of the formation and early evolution of the Milky Way. The bulge GCs (BGCs) are particularly important because they can reveal vital information about the oldest in situ component of the Milky Way.
Aims. Our aim is to derive the mean metallicities and radial velocities for 13 GCs that lie toward the bulge and are generally associated with this component. This region is observationally challenging because of high extinction and stellar density, which hampers optical studies of these and similar BGCs, making most previous determinations of these parameters quite uncertain.
Methods. We used near-infrared low-resolution spectroscopy with the FORS2 instrument on the VLT to measure the wavelengths and equivalent widths of the CaII triplet (CaT) lines for a number of stars per cluster. We derived radial velocities, ascertained membership, and applied known calibrations to determine metallicities for cluster members, for a mean of 11 members per cluster. Unfortunately, one of our targets, VVV-GC002, which is the closest GC to the Galactic center, turned out not to have any members in our sample.
Results. We derive mean cluster RV values to 3 km s^{-1}, and mean metallicities to 0.05 dex. We find general good agreement with previous determinations for both metallicity and velocity. On average, our metallicities are 0.07 dex more metal-rich than those of Harris (2010, arXiv:1012.3224), with a standard deviation of the difference of 0.25 dex. Our sample has metallicities between −0.21 and −1.64, and the values are distributed between the traditional metal-rich BGC peak near [Fe/H] −0.5 and a more metal-poor peak around [Fe/H] −1.1, which has recently been identified. These latter are candidates for the oldest GCs in the Galaxy, if blue horizontal branches are present, and include BH 261, NGC 6401, NGC 6540, NGC 6642, and Terzan 9. Finally, Terzan 10 is even more metal-poor. However, dynamically, Terzan 10 is likely an intruder from the halo, possibly associated with the Gaia-Enceladus or Kraken accretion events. Terzan 10 is also confirmed as an Oosterhoff type II GC based on our results.
Conclusions. The CaT technique is an excellent method for deriving mean metallicities and velocities for heavily obscured GCs. Our sample provides reliable mean values for these two key properties via spectroscopy of a significant number of members per cluster for this important yet previously poorly studied sample of BGCs. We emphasize that the more metal-poor GCs are excellent candidates for being ancient relics of bulge formation. The lone halo intruder in our sample, Terzan 10, is conspicuous for also having by far the lowest metallicity, and casts doubt on the possibility of any bona fide BGCs at metallicities below about −1.5.

Key words. Galaxy: abundances – galaxies: bulges – galaxies: clusters: general

1. Introduction

The formation and evolution of the Milky Way bulge has long been of salient astrophysical interest, both in the context of the Milky Way itself and to understand how our bulge relates to similar structures in other galaxies 9 (see, e.g., Gonzalez et al. 2016; Barbuy et al. 2018a; Saviane et al. 2020, and references therein). We now believe that our bulge formed via several processes. On the one hand, a pressure-supported component formed in situ at the beginning of the Milky Way's assembly, which is the classical, spheroidal bulge, containing a small fraction of the bulge total mass (∼1% as indicated by old and metal-poor RR Lyrae, for example). Later, the boxy-peanut or X-shaped bulge-bar was formed outside-in from instabilities in the inner disk, which contained most of the bulge mass (∼90% as indicated by red clump giant stars), leading to a present-day bulge displaying evidence of

⋆ Full Table 2 is only available at the CDS via anonymous ftp to cdsarc.cds.unistra.fr (130.79.128.5) or via https://cdsarc.cds.unistra.fr/viz-bin/cat/J/A+A/669/A115

both processes (see, e.g., Babusiaux et al. 2010, Zoccali & Valenti 2016, Barbuy et al. 2018a and references therein).

This evidence comes from a variety of tracers. RR Lyrae stars represent the old stellar populations of the bulge and display a spheroidal distribution. Additionally, their metallicities peak around [Fe/H] = −1.0 (Dékány et al. 2013, but see also Pietrukowicz et al. 2015). Red clump stars, with a wider range of age sensitivity, show a bimodal bulge, with two main components: metal-poor stars are more concentrated in a spherical shape and with slower rotation, whereas metal-rich stars are distributed in a boxy shape with a faster rotation (e.g., Kunder et al. 2016; Zoccali et al. 2017). Lastly, GCs are also excellent tracers of the oldest stellar populations in the Galactic bulge. True BGCs most likely formed in situ well before the formation of the bar (Bovy et al. 2019) and stayed confined within the bulge. By the time the bar buckled into a boxy-peanut shape, it trapped the existing BGCs of all metallicities within the inner bulge (Rossi et al. 2015; Bica et al. 2016). Their orbits, and likely also metallicity, distinguish them from thick-disk or inner halo GC intruders (Pérez-Villegas et al. 2020). Therefore, it is important to analyze the metallicity and kinematics of the bona fide BGCs to provide further constraints on the formation and extension of the classical spheroidal component of the Galactic bulge.

It has been known for decades that Galactic GCs can be separated into two populations in terms of their metallicity and spatial distributions: a more metal-poor ([Fe/H] ∼ −1.6) halo component, and a more metal-rich ([Fe/H] ∼ −40.6) centrally concentrated disk–bulge component (Zinn 1985; Minniti 1995; Dias et al. 2016a). Unfortunately, detailed observations of this latter component have been severely limited due to extinction, especially in the optical. Nevertheless, with the advent of infrared detectors and dedicated surveys like the Vista Variables in the Via Lactea (VVV; Minniti et al. 2010) and the Apache Point Observatory Galactic Evolution Experiment (APOGEE; Majewski et al. 2017), it is now possible to observe in much greater detail GCs located toward the bulge. Such observations have suggested an additional subpopulation of bulge GCs, with metallicities substantially below those of the traditional bulge population, with a peak around [Fe/H] ∼ −1.1 (Barbuy et al. 2006, 2009; Bica et al. 2016; Barbuy 2018), but sharing similar chemical and dynamical patterns (Barbuy et al. 2018b, Fig. 12). There may be another population of BGCs with even lower metallicities. Pérez-Villegas et al. (2020) find a small peak around [Fe/H] ∼ −1.5. Many of these intermediate and lower metallicity BGCs also have a blue horizontal branch, which makes them excellent candidates for the oldest GCs (Lee et al. 1994; Dias et al. 2016a) in the Milky Way, with ages approaching the age of the Universe (Kerber et al. 2019). Without invoking HB models, it was recently observationally confirmed that BGCs with blue HBs for their metallicity are quite old, with remarkable consistency; Cohen et al. (2021) found a mean age of 12.9±0.4 Gyr for eight BGCs.

Interestingly, the latest study of bulge field stars, which now includes high-resolution, high S/N spectra of many thousands of genuine bulge stars, also reveals a trimodal metallicity distribution (Rojas-Arriagada et al. 2020). However, the peaks are significantly offset from those of the BGCs, with means of +0.32, −0.17, and −0.66. Clearly, it is important to enhance the number of BGCs with accurate metallicities as well as velocities, both of which are only poorly known in general. In addition to deriving the key parameters for these clusters to improve our limited knowledge of them, this will help us derive a definitive BGC metallicity distribution (MD) to compare to its field star counterpart, select a larger population of GCs of relatively low metallicity which are the best relics to explore the ancient bulge component, investigate the origin of BGCs by determining their orbits by combining accurate radial velocities with the exquisite *Gaia* proper motions, and identify possible halo interlopers within the BGC census.

As noted, extinction is a big challenge for optical high-resolution spectroscopy of BGCs, which is traditionally the best source of accurate metallicities. The advent of the APOGEE-2 main survey and the complementary bulge Cluster APOgee Survey (CAPOS; Geisler et al. 2021, hereafter G21) have gone a long way to help alleviate our previous lack of knowledge of key parameters for a number of BGCs, using near-infrared high-resolution spectroscopy to derive metallicities, chemical abundances, and velocities. Another successful alternative is using low-resolution optical spectroscopy that can reach higher signal-to-noise ratios than high-resolution spectroscopy using similar or shorter exposure times. Dias et al. (2016a) increased significantly the number of bulge GCs with known spectroscopic metallicities, in particular extending and superseding the previously adopted metallicity scale for GCs (Carretta et al. 2009) by adding metal-rich GCs to the homogeneous sample.

Another complementary technique uses the near-infrared CaII triplet (CaT) lines as metallicity indicators. This is a very efficient way to build up a large sample of accurate metallicity and velocity measurements in BGCs. The CaT technique has many advantages. The brightest stars in clusters older than ∼1 Gyr are the red giants, and are thus the natural targets for precision measurements of cluster abundances and velocities. The CaT lines are extremely strong and near the peak flux of unreddened RGB stars, and the technique only requires low resolution ($R \sim 3000$). Because there are many giants in a typical GC, the derived mean abundance can be made much more robust than that based on only one or a few stars, taking advantage of a multiplexing spectrograph. A reasonable sample of stars must also be observed in order to ensure sufficient cluster members, especially in BGCs where (for observations taken prior to *Gaia* results, such as these) membership on the bright RGB may be as low as 20 % due to field contamination (Saviane et al. 2012). This technique can derive metallicities even in the most extincted areas of the Galactic bulge. Many authors have confirmed the accuracy and repeatability of CaT abundance measurements in combination with broadband photometry and shown its very high sensitivity to metallicity and insensitivity to age (e.g., Cole et al. 2004).

In view of all of these advantages, many BGCs have now had a sample of their RGB stars observed using CaT (Rutledge et al. 1997; Saviane et al. 2012, hereafter S12; Mauro et al. 2014, hereafter M14; Vásquez et al. 2018, hereafter V18). However, when we began this study, only about half of the known sample of BGCs had been observed, and we successfully proposed to investigate the remaining sample, with the main goal of completing the sample, essentially doubling the number of bulge GCs with metallicities and velocities from CaT. In particular, the present sample also includes VVV GC002, Terzan 1, Terzan 2, Terzan 6, Terzan 9, Djorg 2, NGC 6401, and NGC6642, GCs that are deemed to have the closest perigalactica to the Galactic center (Minniti et al. 2021a).

This paper is organised as follows. In Sect. 2 we present our cluster sample and describe our target selection. Sect. 3 discusses the observations and reduction procedure. The measurement of velocities and equivalent widths using the CaT lines is given in Sect. 4. Section 5 describes the membership selection and metallicity derivation. We compare our results with previous literature values in Sect. 6. Section 7 discusses the nature of our sample

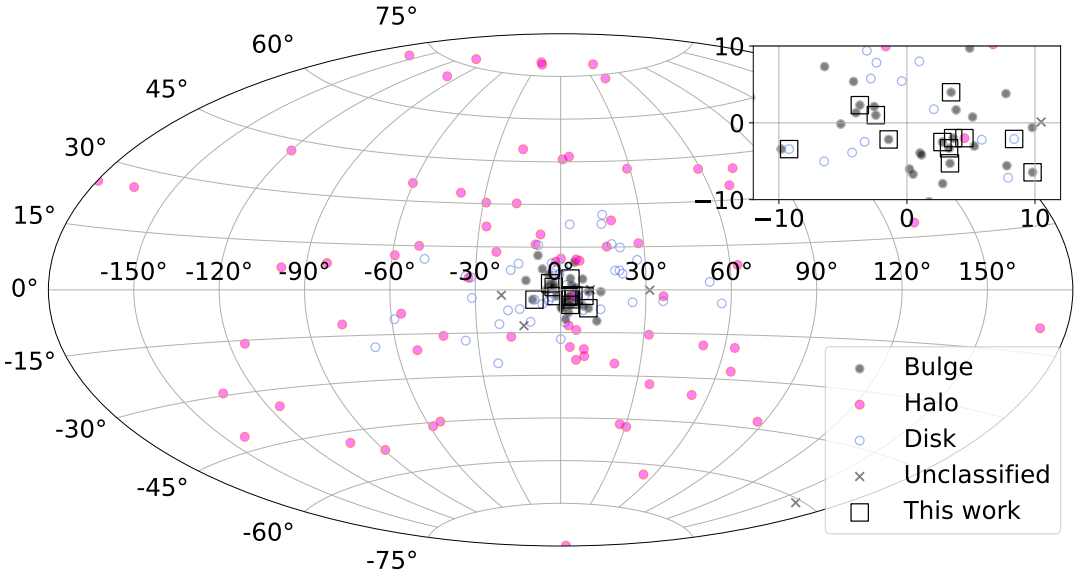

Fig. 1. Aitoff distribution in Galactic coordinates of all Milky Way GCs from the Harris catalog. The classification of Bulge, Disk, and Halo comes from Dias et al. (2016a), updated with the classification by Pérez-Villegas et al. (2020) when available, and are indicated by colored circles (see lower inset). The GCs studied in this work are highlighted with squares. The upper inset shows a zoomed-in region around the GCs analyzed in this work. Assuming this classification, nine GCs belong to the bulge, two to the disk, and one to the halo.

and the bulge MD, and we close our paper with the main conclusions in Sect. 8.

2. Cluster sample and target selection

Our original targets included all GCs appearing within the VVV survey that had not yet had spectra of individual stars obtained at the time of our observing (begun around June 2012). These objects were obvious choices, given their central location in the bulge and the fact that the VVV photometry provided everything required to carry out a successful spectroscopic program, including CMD and radial profile information used to select stars, the astrometry needed to position the slits (thus obviating the need for large-overhead pre-images), and the photometry used to calibrate the CaT technique. A total of 17 GCs were targeted, including principally GCs from the catalog of Harris (1996; version 2010; Harris 2010, hereafter H10) but also two GCs discovered early during the course of the VVV survey: VVV CL001 (Minniti et al. 2011) and VVV CL002 (Moni Bidin et al. 2011). These two clusters are particularly interesting: VVV CL001 appears to be the most metal-poor surviving GC in the inner Galaxy (Fernández-Trincado et al. 2021) and VVV CL002 is the closest known GC to the Galactic center (Minniti et al. 2021a).

During our first allocation, spectra for only four GCs of our sample were obtained, and we subsequently proposed to finish our program the following year. However, in the interim we became aware that a competing program had obtained data for several of our original targets, which we then eliminated from our list. In addition, data for one of our original targets, 2MS-GC02, had a very low S/N, despite having the longest integration, and so we also eliminated this cluster. Data for the remaining 14 GCs observed during the two runs were obtained as described below. The results for one of our samples, VVV CL001, are given in a companion paper and this cluster is not discussed further here. The GCs analyzed in this work are identified in Fig. 1. We note that the main reason that our clusters received little attention before is that they are among the most

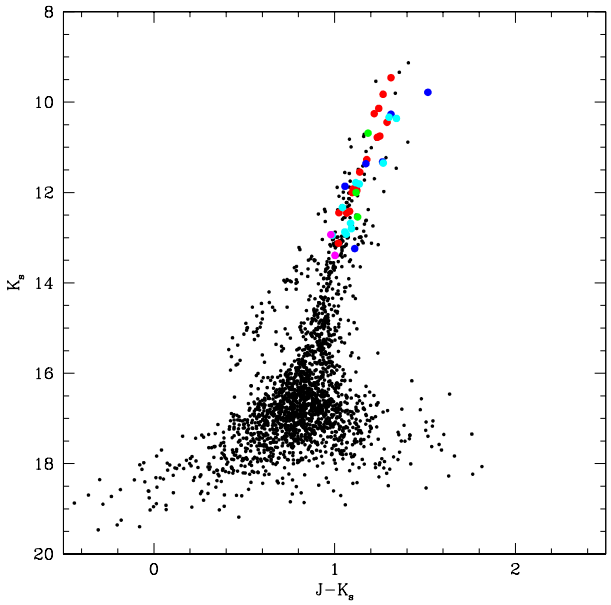

Fig. 2. Color Magnitude Diagram of the cluster NGC 6401. Large symbols represent our spectroscopic targets colored according to our membership classification. Blue symbols represent non-members located beyond the adopted cluster radius. Cyan, green and pink symbols are stars discarded because they have incompatible radial velocities, metallicities or proper motions, respectively. Red points are the stars adopted as final cluster members.

reddened GCs in the Galaxy, with $E(B-V)$ estimates ranging up to almost 3.

The individual spectroscopic targets are red giant stars selected from the cluster VVV CMDs (see Fig. 2). Bright relatively isolated stars lying along the principal RGB and close to the cluster center were prioritized. As noted above, our observations long preceded *Gaia* data, so unfortunately no proper motions were available to help select members at this stage.

3. Observations and reduction

Using the FORS2 instrument (Appenzeller et al. 1998) on the Very Large Telescope (Paranal, Chile), we obtained spectra of ∼540 red giant stars. Observations were performed as part of the programs 089.D-0392 and 091.D-0389 (D. Geisler PI) in service mode. We used FORS2 in mask exchange unit mode, with the 1028z+29 grism and OG590+32 filter. FORS2 has two CCDs (2000×4000 pixels each detector): the master and the secondary chips, which have a readout noise of 2.9 and 3.15 electrons, respectively, and a gain of 0.7 e^- ADU. In most cases, the cluster was observed on the master CCD, while the secondary detector was used for observations of field stars. In a few exceptions (Terzan 9 and Terzan 12), the cluster occupied part of both CCDs. We located between 33 and 66 slits in each total frame (master + secondary CCDs), 1″ wide and 4–8″ long. Pixels were binned 2×2, yielding a plate scale of 0.25″ pixel^{-1}, and a dispersion of ∼0.85 Å pixel^{-1}. The resulting spectra cover a range of 1750 Å(7750–9500 Å), with a central wavelength of 8600 Å, coincident with the region of the CaT lines. The relevant information is given in Table 1, where we include the cluster ID, equatorial coordinates, the K_s magnitude of the red horizontal branch, derived from the VVV data (see below), and the reddening.

The pipeline provided by ESO (version 2.8) was used to perform the bias, flatfield, distortion correction, the wavelength calibration, extraction and the sky subtraction. IRAF was also used for the combination of the spectra (*scombine* task) and the normalization of the combined spectra (*continuum* task).

4. Radial velocity and equivalent width measurements

We measured the radial velocities (RVs) of our targets following the method used by our group in previous work employing the CaT (e.g., Parisi et al. 2015, 2016, 2022). The *fxcor* task was used to perform cross-correlation between the observed stars and the spectra of template stars (Cole et al. 2004) belonging to Galactic open and globular clusters. As the final RV we adopted the average of the cross-correlation results. The correction for the effect introduced by the offset between the star and slit centers is explained in detail in Parisi et al. (2009). We obtained a total error of 7.5 km s^{-1} for our RVs, which is the sum in quadrature between the typical standard deviation of the different cross-correlations (6 km s^{-1}) and the error in centering the image in the spectrograph slit (4.5 km s^{-1}).

Equivalent widths (EWs) were measured on the normalized combined spectra by fitting a combination of a Gaussian and a Lorentzian function. As shown by several authors (e.g., Cole et al. 2004, hereafter C04), such a function reproduces more accurately the center of the line and the wings. We used the bandpasses from Vásquez et al. (2015, hereafter V15; see their Table 1), which modify the wavelength ranges defined by Armandroff & Zinn (1988), in order to better fit the wings and to be fully consistent with the CaT metallicity calibration of V15 and V18 that we follow here. We also measured the EWs using the original definitions by Armandroff & Zinn (1988) in order to be fully consistent with the metallicity calibration of C04 and Dias & Parisi 2020 (hereafter DP20) that we also investigate. The EWs were measured with errors estimated at between ∼0.1–0.5 Å, depending on the line and the S/N of the spectra.

Even when the same pseudo-continuum and bandpass regions are adopted by two different analyses, small differences may appear between their measured EWs for the same spectrum, as seen in V15, S12, and V18 in comparison with previous work. We decided make a comparison of the EW measurements on some spectra from V18 before applying their calibrations to our EWs to finally derive the metallicities; V18 kindly provided 119 reduced and extracted non-normalised spectra for the clusters Djorg 2, Terzan 1, Terzan 2, Terzan 8, Terzan 9, Ton 2, NGC 6426, NGC 6864, and Pal 10, covering the metallicity range $-2.4 \lesssim$ [Fe/H] $\lesssim -0.2$.

We normalised the spectra of all 119 stars from V18 and measured the EWs with the same pseudo-continuum and bandpass regions, and compared our EWs to theirs. We find a tight correlation between our measurements for this work (hereafter TW) and theirs (corrected to the S12 scale) when comparing the sum of the two strongest lines, with a rms of 0.2, which translates to a typical metallicity error of 0.12 dex. The relation is given in Eq. (1) and displayed in Fig. 3. We then adopted this correction to the sum of the EW of the two strongest CaT lines to calculate metallicities on the scales of V15 and V18:

$$\sum \mathrm{EW_{V18}} = 0.95 \cdot \sum \mathrm{EW_{TW}} + 0.06. \quad (1)$$

The scaling relation given by Eq. (1) translates into a small offset in the final metallicities of about 0.03 dex. We only had spectra from V18; therefore, the equivalent comparisons for V15 and C04/DP20 were not performed. However, based on the above comparison, we infer that any additional systematic errors in the final metallicities using the V15 and C04/DP20 scales should be on the order of 0.05 dex or less.

5. Metallicity determination and membership

It is well known that the sum of the EWs of the CaT lines (ΣEW) correlates with metallicity (Armandroff & Zinn 1988). Based on this relation, the CaT technique was developed and has been widely used over the last decades. However, since ΣEW depends not only on metallicity, but also on effective temperature and surface gravity (Armandroff & Da Costa 1991; Olszewski et al. 1991), different authors have proposed the use of the so-called reduced EW (W'), which removes the dependence on these two last parameters, via its correlation with the magnitude of the observed star or, even better, the difference in magnitude between the observed star and the level of the horizontal branch in a given filter (in our case $K_s - K_{s,\mathrm{HB}}$). Many studies have calibrated the ΣEW with metallicity for different filters (see DP20 for a detailed description of the available calibrations). We decided to use the calibration of V18 based on the metallicity scale of Dias et al. (2016a,b), which is the most up-to-date scale for Milky Way globular clusters in the whole metallicity range including metal-rich bulge clusters. We also used the calibrations of V15 and DP20 (that follow C04) for comparison purposes.

For our individual targets, we adopted the K_s magnitudes from the VVV survey (Minniti et al. 2010). For our cluster sample, we followed the procedure described in M14 in order to calculate the $K_{s,\mathrm{HB}}$. The magnitude at the HB level was determined by the position of the peak in the luminosity distribution of the reddest part of the HB. To improve the peak determination, we started from initial guesses obtained from several sources, such as the values presented in Valenti et al. (2007, 2010). For some clusters, we calculated a "theoretical" value based on data from Bressan et al. (2012) and Girardi & Salaris (2001), corrected for distance modulus and reddening of the GC. An empirical value was also calculated from the V_{HB} value listed in H10, corrected for distance modulus and reddening of the GC, and for a mean $(V - K_s)$ color determined using Bressan et al. (2012). The accuracy of these two methods strongly depends on the accuracy of the known photometric parameters of the

Table 1. Observed bulge globular clusters.

Cluster	Alternative designation	RA J2000	Dec J2000	$K_{s,\mathrm{HB}}$ mag	$E(B-V)$ (*)
BH 261	AL 3 ESO 456-78 MWSC 2847	18 14 06.6	−28 38 06	12.85 ± 0.10	0.36
Djorg 2	ESO 456-38 MWSC 2779	18 01 49.1	−27 49 33	12.92 ± 0.10	0.94
NGC 6401	ESO 521-11 MWSC 2653	17 38 36.6	−23 54 34	13.17 ± 0.05	0.72
NGC 6540	Djorg 3 BH 258 MWSC 2804	18 06 08.6	−27 45 55	12.64 ± 0.05	0.66
NGC 6642	ESO 522-32 MWSC 2941	18 31 54.1	−23 28 31	13.14 ± 0.04	0.40
Terzan 1	ESO 455-23 Haute-Provence 2 BH 235 MWSC 2635	17 35 47.2	−30 28 54	13.45 ± 0.10	1.99
Terzan 2	ESO 454-29 Haute-Provence 3 BH 228 MWSC 2600	17 27 33.1	−30 48 08	13.70 ± 0.05	1.87
Terzan 6	ESO 455-49 Haute-Provence 5 BH 249 MWSC 2719	17 50 46.4	−31 16 31	13.80 ± 0.10	2.35
Terzan 9	MWSC 2778	18 01 38.8	−26 50 23	13.00 ± 0.10	1.76
Terzan 10	ESO 521-16 MWSC 2793	18 02 57.4	−26 04.00	13.45 ± 0.10	2.40
Terzan 12	Terzan 11 ESO 522-1 MWSC 2838	18 12 15.8	−22 44 31	12.83 ± 0.10	2.06
Ton 2	Pismis 26	17 36 10.5	−38 33 12	13.49 ± 0.05	1.24
VVVCL002		17 41 06.3	−28 50 42	13.80 ± 0.15	2.88

Notes. (*)From H10.

cluster. Unlike the sample of M14, the clusters analyzed in this work are affected by higher extinction and greater differential reddening, and more contamination by field stars. To best estimate the peak in the luminosity distribution of the reddest part of the HB, for each cluster we produced color–magnitude diagrams (CMDs) and Hess diagrams for different cuts in distance from the cluster center (typically 30′, 60′, and 90′). For each cut we selected comparison fields covering an equal area. We scrutinized these CMDs and Hess diagrams to determine which overdensities belong to the cluster and which to the surrounding environment, for example the Galactic bulge or spiral arms. For Terzan 10, a cluster particularly affected by differential reddening, we based our estimations mainly on the values given by Alonso-García et al. (2015).

The slope β of the relation between magnitude and $\sum$EW, needed to correct for temperature and luminosity effects, varies with the adopted filter and with the number of lines considered in $\sum$EW. V15 found $\beta_{\mathrm{Ks}} = 0.384 \pm 0.019$, which we also use to calculate metallicities on the V15 scale. V18 found $\beta_{\mathrm{V}} = 0.55$, which is converted to K_s using the recipes by DP20, deriving $\beta_{\mathrm{Ks}} = 0.37$. We note that V18 is on the same scale as S12, and M14 found $\beta_{\mathrm{Ks}} = 0.385 \pm 0.013$. Therefore, β is very consistent among these calibrations, all using the two strongest CaT lines. In the case of the C04 scale, they used all three CaT lines and the V filter, with $\beta_{\mathrm{V}} = 0.73 \pm 0.04$, which was fitted by DP20 resulting in $\beta_{\mathrm{V}} = 0.71 \pm 0.05$ and $\beta_{\mathrm{Ks}} = 0.48 \pm 0.06$.

The reduced EW calculated for each star on each scale described above is then converted into metallicity following the respective scales, in order to be fully consistent. V15 derived [Fe/H] $= -3.150 + 0.432W' + 0.006W'^2$, V18 derived [Fe/H] $= -2.68 + 0.13W' + 0.055W'^2$, and DP20 derived [Fe/H] $= -2.917 + 0.353W'$.

In order to discriminate between cluster members and surrounding field stars, we applied the same membership determination method used by our group in previous CaT work (Parisi et al. 2009, 2015, 2022; Dias et al. 2021, 2022b), namely the distance of the star from the center of the cluster, its RV, [Fe/H], and proper motion. To be considered a member, a star must satisfy all of the following criteria: 1) it must be within the adopted cluster radius, and so built the radial stellar density profile (see Parisi et al. 2009, 2015, 2022 for more details) in order to determine the radius; 2) it must have an RV that falls within the error plus intrinsic dispersion (generously adopted as

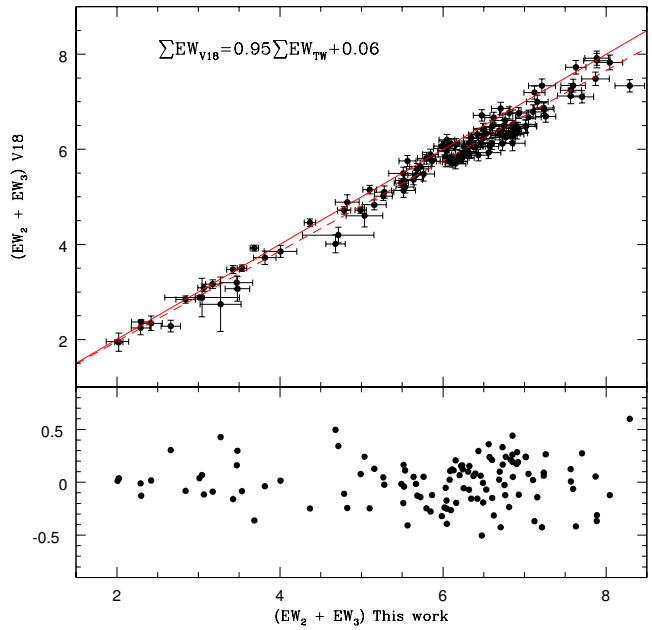

Fig. 3. Sum of the EWs from the two strongest CaT lines (*top panel*), measured by us and by V18 (corrected to the S12 scale). The continuous line shows the one-to-one relation, while the dashed line shows the best-fit relation given by Eq. (1). Residuals of the comparison to the fit are shown in the *bottom panel*.

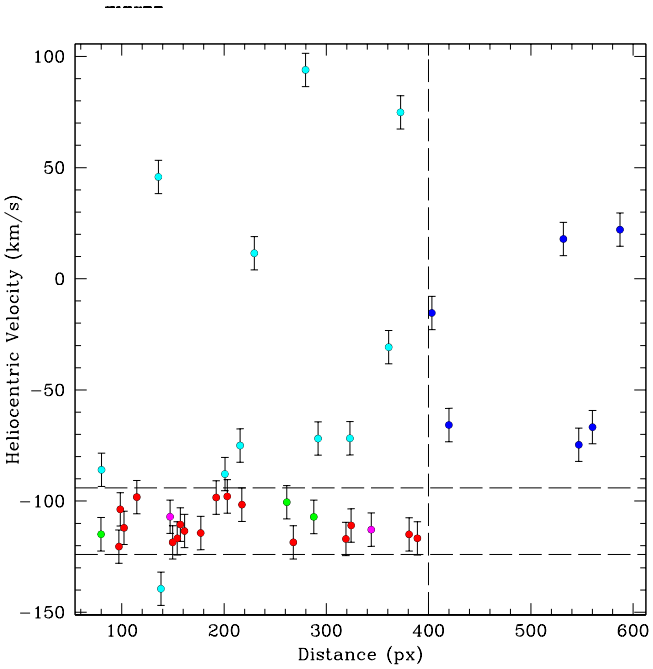

Fig. 5. Heliocentric radial velocity vs. distance from the cluster center for NGC 6401 targets. Symbols are as in Fig. 2. Radial velocity error cuts (±15 km s^{-1}, horizontal lines) and the adopted cluster radius (vertical line) are shown.

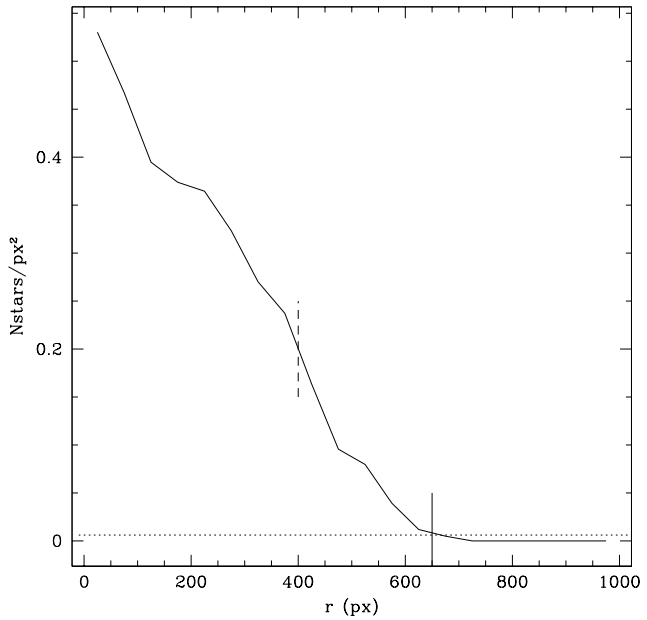

Fig. 4. Radial stellar density profile of the cluster NGC 6401. The horizontal line shows the stellar background level. The solid and dashed vertical lines represent the measured and the adopted cluster radius, respectively.

±15 km s^{-1}) from the cluster mean, and ideally different from the average RV of the surrounding stellar field; 3) it must have an [Fe/H] value within the adopted metallicity cuts (±0.20 dex, given by the mean error in the metallicity determinations) of the mean; and 4) it must have a PM that lies within three standard deviations of the cluster mean. We used the proper motions from the *Gaia* DR3[1] survey (Gaia Collaboration 2021).

[1] https://www.cosmos.esa.int/web/gaia/data-release-3

In Fig. 2 we show the CMD of the cluster NGC 6401 as an example, and in Fig. 4 we show the stellar radial density profile of this cluster. By our definition, the radius of the cluster (solid vertical line in the figure) is the point where the stellar density profile intersects the background level (dotted line). For the present analysis we adopt a more conservative radius (dashed line) to increase the membership probability of the stars adopted as cluster members. We carefully checked that stars with RVs and metallicities compatible with cluster membership had not been discarded due to a very restrictive cutoff in the radius. No additional potential members were found in our sample beyond the adopted radius but within the tidal radius. We note that the structural parameters for most of these clusters are very poorly known. In addition to observational difficulties, many of them are also likely core-collapsed, so they are not well fit by conventional (e.g., King 1966) analytical profiles.

For the same example cluster, we include in Figs. 5 and 6 the behavior of the RV and metallicity with distance from the center, respectively. Fig. 7 show the positions of our targets in the PM plane from *Gaia* eDR3. The color-coding used in these figures is the same as in Fig. 2 and in our previous CaT work (see, e.g., Parisi et al. 2022; Dias et al. 2022b): field stars located at a distance from the cluster center greater than the adopted radius have been plotted in blue; stars discarded because they have RVs or metallicities outside of the adopted cuts are shown in cyan and green, respectively; stars discarded because of their discrepant PMs are in magenta. The red circles represent stars that have passed all the criteria, and are therefore considered our final cluster members.

Unfortunately, the VVV CL002 observations were made long before *Gaia*, and none of our sample of 14 stars observed in this area passed our membership criterion. In particular, all stars fall well away from the cluster mean PM found by Vasiliev & Baumgardt (2021). This is a graphic illustration of the importance of PM in determining cluster membership for

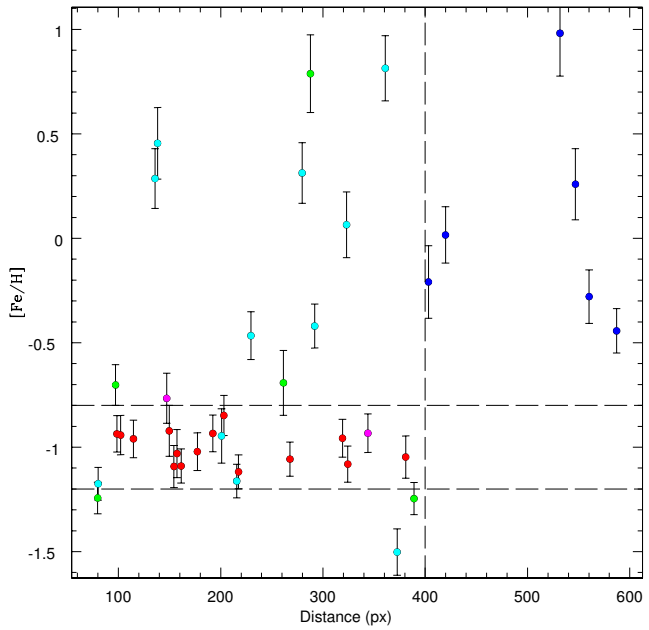

Fig. 6. Metallicity vs. distance from the cluster center for NGC 6401 targets. The color-coding is the same as in Fig. 2. Metallicity error cuts (±0.2 dex, horizontal lines) and the adopted cluster radius (vertical line) are shown.

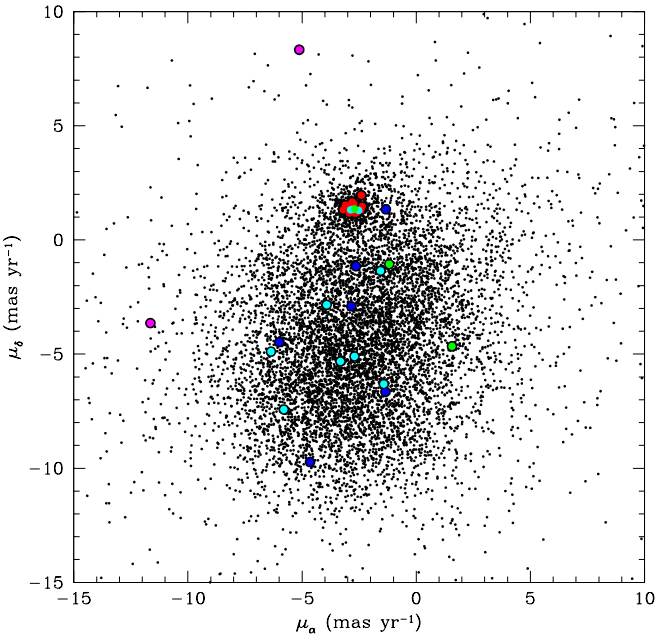

Fig. 7. Proper motion plane for the cluster NGC 6401. The black points represent stars from the *Gaia* eDR3 catalog and the large circles are our spectroscopic targets. The color-coding is the same as in Fig. 2.

such crowded and convolved fields. Thus, VVV CL002 is excluded from further discussion. However, this remains a very interesting target; Minniti et al. (2021a) confirmed that this is a real GC based on the VVV PM diagram, and concluded that it is the closest GC to the Galactic center.

We found a total of 130 members in our remaining 12 clusters, for an average of 11 members per cluster, with the range falling from only 2–3 stars (in BH 261, Djorg 2, and Terzan 6) to 19 in NGC 6642. For our members, we include in Table 2 the star identification, the equatorial coordinates, RV, $K_s - K_s$(HB), ΣEW (for the two strongest lines), and metallicity (corresponding to the V18 calibration), with their respective errors.

In Fig. 8 we show the behavior of ΣEW as a function of $K - K_{s,\mathrm{HB}}$ for targets in NGC 6401; the cluster members follow an iso-abundance line, with a mean metallicity of −1.0. The same can be seen in Fig. 9 for all clusters in our sample, considering only cluster members for each cluster individually. For each cluster, red giants follow lines of equal slope but different zero points, which depends only on the cluster metallicity. This graphically displays the power of the CaT technique to derive metallicity.

Finally, we calculated the cluster mean RV and metallicity on the adopted V18 scale, and on two additional scales, V15 and DP20, for comparison. The results along with their corresponding errors are presented in Table 3. We also include the number of members in each cluster and the mean PM derived, which are in very good agreement with the mean values derived by Vasiliev & Baumgardt (2021) considering the errors. The mean metallicity is typically determined to an internal error of 0.05 dex, while the mean RV has a mean error of 3 km s^{-1}. None of our clusters show strong evidence for a range in metallicities significantly exceeding that expected from the measurement errors, although NGC 6642 and Terzan 6 have a substantially larger range than the other clusters. For the rest of the paper, we utilize our mean metallicity on the V18 scale, following the Dias et al. (2016a,b) metallicity scale as our favored value, as delineated above.

6. Comparison with previous results

All of our clusters have previous determinations of both RV and metallicity. Radial velocities only require, at a minimum, rather low-resolution, low S/N spectra, while metallicities can be derived via a large number of techniques, ranging from broadband photometry to high-resolution, high S/N spectroscopy, and integrated light to individual stars, with a concomitantly wide range of accuracy. We therefore expect that RVs for our sample should generally be in reasonable agreement, although of course the possibility of previous studies including non-members is an issue. It should be noted, however, that although published metallicities exist for all of our sample, they come from a variety of methods, many of which are of rather low quality. This means that these values are both inhomogeneous and quite uncertain in general, especially given the fact that our sample was left relatively unstudied for good reason, namely the high extinction as well as crowding associated with BGCs. We therefore anticipate more significant metallicity discrepancies in our sample.

Here we compare our results with the previous literature values for each cluster in turn. We concentrate on RV and [Fe/H] determinations from five (generally) internally homogeneous, recent, and widely used catalogs, which should help minimize the errors associated with field star inclusion and/or lower quality techniques. These include H10, which in fact is not internally homogeneous or recent, but is regarded as the bible of Galactic GC properties; Vásquez et al. (2018, V18), who used the same CaT technique on a large sample of reddened GCs; Baumgardt et al. (2019, hereafter B19), a catalog of various GC parameters including RV, Dias (2019, hereafter D19)[2], who averaged spectroscopic metallicities from multiple studies when available, after bringing them to the homogeneous metallicity scale of Dias et al. (2016a,b); and Geisler et al. (in prep.,

[2] https://www.sc.eso.org/~bdias/catalogues.html

Table 2. Measured values for member stars.

Star [(*)]	RA J2000	Dec J2000	RV km s^{-1}	$K_s - K_s$(HB) mag	ΣEW Å	[Fe/H] dex
BH261−286607−M−09	18.2345	−28.6465	−52.5 ± 1.9	−0.38 ± 0.10	4.34 ± 0.19	−1.25 ± 0.11
BH261−291014−M−16	18.2352	−28.6349	−42.23 ± 1.2	−2.23 ± 0.10	5.02 ± 0.09	−1.27 ± 0.08
BH261−320470−M−24	18.2358	−28.6232	−39.9 ± 2.3	−0.62 ± 0.10	4.74 ± 0.16	−1.08 ± 0.11

Notes. This table is available in its entirety at the CDS. A portion is shown here for guidance regarding its form and content. [(*)]Cluster name – ID from the photometry – CCD chip (M:master, S: secondary) – aperture number.

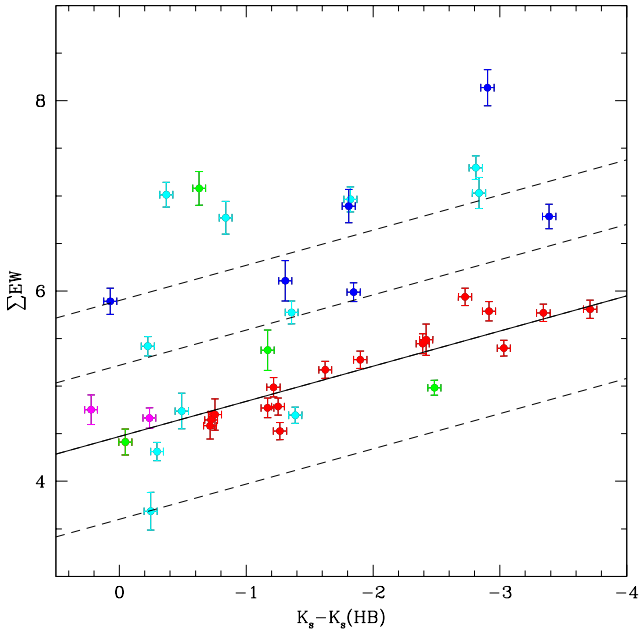

Fig. 8. Sum of the EW of the three CaT lines vs. the difference $K - K_{HB}$ for stars identified as members of NGC 6401. The color-coding is the same as in Fig. 2. The solid line represents a metallicity of −1.0, while the dashed lines represent [Fe/H] = 0.0, −0.5, and −1.5 (*from top to bottom*).

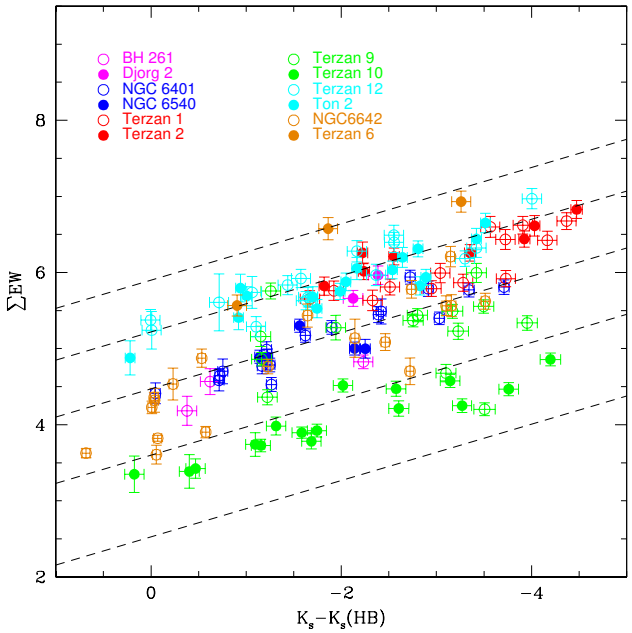

Fig. 9. Same as in Fig. 8, but for members in all clusters. The dashed lines represent [Fe/H] = 0.0, −0.5, −1.0, −1.5, and −2.0 (*from top to bottom*).

hereafter G22), who are studying BGCs with the APOGEE spectrograph in SDSS-IV via the CAPOS project. We note that our sample generally included almost twice as many stars per cluster as either V18 or G22, with the additional benefit that V18 did not have *Gaia* PMs to help select members. We also note that CAPOS is the only source of high-resolution spectroscopic metal abundances (and RVs) for our sample except for Terzan 1, as noted below, while the metallicities from H10 generally come from photometry or, at best, low-resolution spectroscopy. We also note that we used the D16 calibration values from V18. There are no clusters in common with the MUSE CaT sample by Husser et al. (2020) for direct comparison, but they follow Dias et al. (2016a,b); therefore, their results should be on the same scale as ours. All values are listed in Table 4. V18 and G22 also include references to other, generally older and less reliable, RV and metallicity derivations for clusters in common with our sample, which are not discussed in detail here.

BH 261. Our sample is small, only three members. The only published RV measurement, from B19, is in reasonable agreement with our value. All three [Fe/H] values are very similar. No previous CaT or high-resolution studies exist.

Djorg 2. Good to reasonable agreement exists with all previous RV values. Our metallicity is in excellent agreement with H10, but much higher than other determinations, with an offset of about 0.4–0.45 dex with respect to the V18 CaT and G22 CAPOS values, respectively. However, we note that we measured only two members, the smallest number in our sample, while V18 had three members and G22 had six.

NGC 6401. The H10 RV is much higher than our value, which is instead very consistent with that of V18 and B19. Our metallicity value is in good agreement with that of H10 and D19 and in reasonable agreement with V18.

NGC 6540. All RV values are in good agreement, as are the [Fe/H] values, except that of H10, which is in relatively poor agreement. However, this value is based only on the slope of the RGB in the near-IR, a technique of low precision.

NGC 6642. The RVs are in good agreement, although the B19 value is 15 km s^{-1} higher than ours. The metal abundances are all in good to excellent agreement.

Terzan 1. This is a very interesting GC because it is one of the few second-parameter GCs within the bulge, with a red horizontal branch, but a steep red giant branch indicating a rather low metallicity. It has been the subject of several recent studies,

Table 3. Derived cluster mean parameters.

	n	RV km s^{-1}	$[Fe/H]^{(adopted)}_{V18}$ dex	$[Fe/H]_{V15}$ dex	$[Fe/H]_{DP20}$ dex	μ_α mas yr^{-1}	μ_δ mas yr^{-1}
BH 261	3	−44.9 ± 3.8(6.7)	−1.21 ± 0.06(0.10)	−1.19 ± 0.05(0.09)	−1.09 ± 0.05(0.09)	3.52 ± 0.11(0.18)	−3.63 ± 0.16(0.27)
Djorg 2	2	−162.4 ± 9.1(12.9)	−0.67 ± 0.07(0.10)	−0.75 ± 0.05(0.08)	−0.70 ± 0.05(0.07)	0.65 ± 0.03(0.04)	−3.00 ± 0.02(0.03)
NGC 6401	15	−110.8 ± 1.8(7.8)	−1.00 ± 0.03(0.12)	−1.01 ± 0.02(0.10)	−0.91 ± 0.02(0.09)	−2.75 ± 0.06(0.24)	1.43 ± 0.05(0.20)
NGC 6540	5	−22.1 ± 1.3(2.9)	−1.04 ± 0.06(0.14)	−1.05 ± 0.05(0.11)	−0.98 ± 0.04(0.10)	−3.74 ± 0.04(0.08)	−2.74 ± 0.10(0.21)
NGC 6642	19	−48.2 ± 1.8(8.0)	−1.11 ± 0.06(0.24)	−1.11 ± 0.05(0.21)	−1.04 ± 0.04(0.15)	−0.21 ± 0.04(0.18)	−3.86 ± 0.05(0.20)
Terzan 1	13	68.4 ± 3.1(11.2)	−0.71 ± 0.04(0.14)	−0.77 ± 0.03(0.11)	−0.73 ± 0.03(0.11)	−2.84 ± 0.08(0.28)	−4.87 ± 0.10(0.37)
Terzan 2	8	130.5 ± 2.3(6.5)	−0.54 ± 0.03(0.10)	−0.65 ± 0.03(0.07)	−0.56 ± 0.02(0.06)	−2.14 ± 0.03(0.09)	−6.31 ± 0.05(0.13)
Terzan 6	3	134.7 ± 3.4(6.0)	−0.21 ± 0.15(0.25)	−0.42 ± 0.10(0.18)	−0.43 ± 0.08(0.15)	−4.83 ± 0.14(0.25)	−7.25 ± 0.09(0.16)
Terzan 9	14	70.1 ± 2.4(9.0)	−1.15 ± 0.03(0.12)	−1.14 ± 0.03(0.11)	−1.06 ± 0.03(0.10)	−2.16 ± 0.07(0.25)	−7.62 ± 0.06(0.21)
Terzan 10	16	209.3 ± 3.1(12.5)	−1.64 ± 0.02(0.09)	−1.59 ± 0.02(0.08)	−1.47 ± 0.02(0.08)	−6.99 ± 0.12(0.47)	−2.56 ± 0.07(0.28)
Terzan 12	16	107.4 ± 1.7(6.7)	−0.48 ± 0.04(0.15)	−0.60 ± 0.03(0.11)	−0.58 ± 0.03(0.10)	−6.42 ± 0.05(0.21)	−3.09 ± 0.04(0.15)
Ton 2	16	−180.8 ± 2.0(8.1)	−0.57 ± 0.03(0.13)	−0.67 ± 0.02(0.10)	−0.61 ± 0.03(0.10)	−5.97 ± 0.04(0.15)	−0.81 ± 0.03(0.12)

Notes. Errors correspond to the standard error of the mean (values in parentheses are the standard deviation).

which makes it a good target for comparison among the different techniques, both in RV and in metallicity.

The first RV published for Terzan 1 was 35 km s^{-1}, based on integrated CaT spectroscopy (Armandroff & Zinn 1988). We suspect this relatively low value compared to all the subsequent measurements is due to field star contamination. The Valenti et al. (2015) high-resolution spectroscopy gave an average RV = 57±1.8 km s^{-1}, which is offset by about 11 km s^{-1} from our value. Vásquez et al. (2018) derived 63±0.5(8) km s^{-1}, based on nine stars, which is consistent with both the high-resolution result and our value.

Baumgardt & Hilker (2018) analyzed our FORS2 data for Terzan 1. They reduced the spectra, measured the RVs, and estimated the cluster membership based only on RV information, deriving a mean of RV = 57.7±1.2 km s^{-1}, more than 10 km s^{-1} lower than our value of RV = 68.4±3.1 km s^{-1}, which is surprising given the identical data and estimated errors. We find that there are a number of stars with RVs similar to the confirmed members, but with different metallicities and proper motions. Therefore, Baumgardt & Hilker (2018) ended up including a number of non-members since they did not take into account metallicity and proper motion, which we used in our membership selection. This incompatible membership selection likely explains the difference in the mean cluster RV obtained by the two studies based on the same data (see Tables 3 and 4). This comparison shows the danger of defining GC membership using only RV. In cases where the contrast with the field is small, the average RV will not suffer much, but of course metallicity could suffer, and in the case of low-mass GCs in a dense field, RV alone is not enough to assess membership. Finally, Idiart et al. (2002) derived a mean RV = 114±14 km s^{-1}, which is what the H10 value is based on. This has a very significant offset with respect to all the other values. Valenti et al. (2015) had member stars in common with Idiart et al. (2002) with similar metallicities but discrepant RV, and argued that the RV offset is probably related to some systematic errors not accounted for in Idiart et al. (2002).

Ortolani et al. (1999) and Valenti et al. (2010) derived a metallicity around −1.1 from optical and near-IR photometry, respectively. The metallicity given by H10 of [Fe/H] = −1.03±0.03 dex agrees with these values. It comes from the average of the integrated low-resolution CaT metallicity by Armandroff & Zinn (1988) of [Fe/H] = −0.71±0.15 dex on the Zinn & West (1984) metallicity scale or [Fe/H] = −0.68±0.15 dex in the Carretta et al. (2009) metallicity scale, and the average low-resolution optical spectroscopic metallicity from seven RGB stars of −1.27±0.05 dex by Idiart et al. (2002). More recently, Valenti et al. (2015) used high-resolution H-band spectroscopy to find −1.26±0.03 dex based on 15 members, some of them in common and in agreement with Idiart et al. (2002). Vásquez et al. (2018) used the same technique as we do here, and presented final average metallicities based on nine stars: $[Fe/H]_{D16}$ = −0.74±0.18 dex, which resembles the higher metallicities derived from integrated CaT spectra, as we also find here: $[Fe/H]_{V18}$ = −0.71±0.04 dex. Vásquez et al. (2018) argued that the HB magnitude was very uncertain in the V filter because of differential reddening, increasing the uncertainty in metallicity to about 0.15 dex. In summary, three studies based on CaT agree on a higher metallicity than that found by photometry and high-resolution spectroscopy. Potentially, the difference could be related to the high α-element abundance of this GC (∼0.4 dex, Valenti et al. 2015), which makes the overall metallicity increase by about ∼0.2 dex with respect to [Fe/H] (i.e., [M/H] = −0.91; Valenti et al. 2010).

Terzan 2. Our RV is in excellent agreement with B19 and G22, in rough agreement with V18, and in poor agreement with H10. We note that V18 only included three members while we have eight. We find good agreement with other metallicities except for G22, which is again about 0.35 dex lower than our determination.

Terzan 6. Our sample is small, only three members. Very good agreement exists with both previous RV determinations. However, our [Fe/H] value is more than 0.3 dex higher than the H10 and D19 values. Both of these metallicities are based only on the near-IR RGB slope. The largest metallicity difference among the three scales in Table 3 is for this cluster, amounting to 0.22 dex, and this is also the highest metallicity cluster in our sample by a substantial amount. The difference is expected because the calibration by V18, based fully on globular clusters by Dias et al. (2016a,b), differs from V15 only in the metal-rich regime. The argument in V18 was that their calibration is based only on globular clusters including metal-rich bulge GCs, whereas V15 relied on bulge field stars for the metal-rich regime. Therefore, we kept our choice for the metallicity following V18 in Table 3.

Terzan 9. Very good agreement is found with all RV values, with the notable exception of B19, whose value is more than 40 km s^{-1} lower than ours. Excellent metallicity agreement exists, with the notable exception of G22, which again is about 0.25 dex lower than our determination. We note that Ernandes et al. (2019) carried out low-resolution VLT-MUSE

observations and derived a mean RV of 58.1 ± 1.1 km s^{-1} and mean [Fe/H] = −1.10±0.15 from a large number of stars, in good agreement with our values.

Terzan 10. The only previous RV measurement is that of B19, whose value of −64.11±3.09 km s^{-1} is over 270 km s^{-1} lower than ours. This is by far the largest discrepancy in our comparison. We note that our sample includes 16 members and that our error is very reasonable, and also that we do not find any stars with RVs between 0 and −100 km s^{-1} in our sample of 46 stars (including the secondary chip). Thus, we strongly suspect that there is an error in the B19 value. They have recently updated their determination in their personal website[3] to 211.37±2.26 km s^{-1}, which is now in very good agreement with our determination. The metallicity agreement is also the worst of all our clusters, with a discrepancy of almost 0.7 dex. However, both the H10 and D19 values are based only on the RGB slope in the $V-I$ color, which is even more susceptible to errors such as reddening than the near-IR technique. This cluster suffers from extreme differential extinction, as seen in Alonso-García et al. (2015) and Cohen et al. (2018), which is undoubtedly at least partly to blame for the above discrepancies. Moreover, Alonso-García et al. (2015) studied variable stars in Terzan 10 and found that based on their periods combined with the [Fe/H] ∼ −1.0 from H10, this cluster lies between Oosterhoff groups II and III. Spectroscopic metallicity was required for a definitive classification: [Fe/H] ∼ −0.5 would mean a rare case of Oosterhoff III, and [Fe/H] ≲ −1.5 would mean Oosterhoff II. We find [Fe/H]= −1.64, finally resolving this uncertainty, as already mentioned by Alonso-García et al. (2021) based on our preliminary results.

Terzan 12. Reasonable RV agreement is found, as well as excellent metallicity agreement, with the H10 and D19 values, based only on the VI RGB slope.

Ton 2. We find very good agreement among the variety of RV derivations, while the metallicity values are either close to ours (H10 and G22) or about 0.3 dex higher. We note that Fernández-Trincado et al. (2022) find very similar results to G22 from essentially the same sample.

Comparing our RVs to previous determinations, we find a mean difference (our value minus the previous value) of −3.2±25.1 km s^{-1} for 9 clusters in common with H10, −2.8±7.5 km s^{-1} for 6 clusters in common with V18, +23.3±80.3 km s^{-1} for 12 clusters in common with B19, and −2.9±6.2 km s^{-1} for 6 clusters in common with G22. All of these differences are quite reasonable except with B19, which in fact is now generally regarded as the most reliable compilation. However, as noted above, there are two very strong outliers in our comparison with B19: Terzan 9 and 10. If we eliminate these two, we find a mean difference of only −3.4±10.6 km s^{-1} for the other ten clusters. Thus, overall agreement with prior published values is good, but does suggest our values are about 3 km s^{-1} too low on average. Another explanation is that the uncertainties are slightly underestimated.

For the metallicities we find a mean difference (as above, adopting [Fe/H]$_{V18}$) of +0.07±0.25 dex for 12 clusters in common with H10, 0.00±0.20 dex for 6 clusters in common with V18, −0.06±0.25 dex for 12 clusters in common with D19, and +0.22±0.16 dex for 6 clusters in common with G22. We note the very good agreement with V18, as expected, because by construction our metallicity determinations are on the same scale, which is generally compatible with high-resolution spectroscopy and with H10. This is also true of D19, but the agreement is not as good. The large offset from G22 is somewhat surprising. We note again that our sample size is on average almost twice that of G22 for the clusters in common. However, G22 did have the benefit of *Gaia* proper motions as a membership criterion, and also use high-resolution spectroscopy, which should yield more robust metallicities compared to our CaT technique. We found however that the large offset is the average of a small offset of +0.11±0.12 dex from three clusters and a large offset of +0.32±0.13 dex from the other three clusters; therefore, the large offset may be due to something particular to these three clusters. Two of them are by far the most reddened of the six. Nidever et al. (2020) compare the metallicities of stars in 26 GCs with APOGEE ASPCAP metallicities ranging from −0.6 to −2.3 with those of other high-resolution studies, and found a mean offset of 0.06 dex to higher metallicity for APOGEE and a scatter of 0.09 dex, while Fernández-Trincado et al. (2020) find an offset of 0.11±0.11 dex in the opposite sense when comparing ASPCAP to BACCHUS abundances. Thus, the cause of this discrepancy may be related to different techniques to analyze APOGEE spectra combined with some challenges in three particular GCs.

7. Bulge globular clusters

7.1. Nature of our sample

Since the pioneering work of Shapley (1918), it has been recognized that the GCs of our Galaxy have a strong central concentration. The density may increase within a few kpc of the Galactic center, suggesting possibly distinct outer (halo) and inner (bulge) groups.

Zinn (1985) first posited the existence of separate halo and disk populations of GCs based on their distinct spatial and MD. From existing information on metallicity, scale height, and rotational velocities available at that time, Armandroff (1989; and references therein) interpreted a sample of low Galactic latitude metal-rich GCs as belonging to a disk system. However, Minniti (1995), from metallicity and kinematics of GCs in the central 3 kpc, suggested that these GCs instead constitute a bulge population. This was corroborated by Côté (1999), who used spectroscopic metallicities and RVs for GCs within 4 kpc of the Galactic center. The issue of whether there is a single bulge–(thick)disk population or if they are distinct has been discussed for several decades (see, e.g., Harris 2001).

As recently as a few years ago, the review of Bica et al. (2016) left this question still somewhat open. They defined BGCs as those with $R_{GC} < 3$ kpc and [Fe/H] ≥ −1.5 and found 43 such GCs in the H10 catalog. However, they also realized that these limits were somewhat arbitrary and admitted the possibility of these exceptions as halo intruders with low metallicities that are at the moment simply passing through the bulge near their perigalacticon (e.g., VVV CL001, Fernández-Trincado et al. 2021) or as metal-rich GCs lying beyond the radial limit, which overlap with Armandroff's disk GCs, but that did not have existing space velocities available at the time, prohibiting a more precise characterization.

With the advent of the exquisite proper motions provided by *Gaia*, our ability to characterize GCs has been revolutionized by adding the powerful dimension of kinematics and dynamics. We now realize, in large part thanks to *Gaia*, that not only can GCs be classified as halo, bulge, or disk, but that indeed we can

[3] https://people.smp.uq.edu.au/HolgerBaumgardt/globular/fits/ter10.html

Table 4. RV and metallicity from five internally homogeneous GC catalogs for our BGCs.

Name	RV (km s^{-1})	[Fe/H]	Source
BH 261	–	−1.30	H10
“	−29.38 ± 0.60	–	B19
“	–	−1.27 ± 0.16	D19 (**)
Djorg 2	–	−0.65	H10
“	−159.9 ± 0.9	−0.97 ± 0.13	V18
“	−148.05 ± 1.38	–	B19
“	–	−0.91 ± 0.05	D19
“	−152.0 ± 1.2	−1.14 ± 0.04	G22
NGC 6401	−65.0 ± 8.6	−1.02	H10
“	−115.4 ± 0.8	−1.18 ± 0.14	V18
“	−99.26 ± 3.18	–	B19
“	–	−1.08 ± 0.06	D19
NGC 6540	−17.7 ± 1.4	−1.35	H10
“	−17.98 ± 0.84	–	B19
“	–	−0.89 ± 0.73	D19
“	−14.4 ± 1.1	−1.09 ± 0.06	G22
NGC 6642	−57.2 ± 5.4	−1.26	H10
“	−33.23 ± 1.13	–	B19
“	–	−1.03 ± 0.17	D19
“	−55.4 ± 2.4	−1.11 ± 0.04	G22
Terzan 1	114 ± 14	−1.03	H10
“	63.0 ± 1.5	−0.74 ± 0.18	V18
“	57.55 ± 1.61	–	B19
“	–	−0.74 ± 0.09	D19
Terzan 2	109.0 ± 15.0	−0.69	H10
“	144.6 ± 1.4	−0.42 ± 0.18	V18
“	128.96 ± 1.18	–	B19
“	–	−0.42 ± 0.21	D19
“	134.1 ± 1.1	−0.88 ± 0.02	G22
Terzan 6	126.0 ± 15.0	−0.56	H10
“	137.15 ± 1.7	–	B19
“	–	−0.53 ± 0.16	D19 (**)
Terzan 9	59.0 ± 10.0	−1.05	H10
“	71.4 ± 1.0	−1.08 ± 0.14	V18
“	29.31 ± 2.96	–	B19
“	–	−1.08 ± 0.16	D19
“	69.8 ± 5.1	−1.42 ± 0.04	G22
Terzan 10	–	−1.00	H10
“	−64.11 ± 3.09	–	B19
“	–	−0.97 ± 0.16	D19 (**)
Terzan 12	94.1 ± 1.5	−0.50	H10
“	94.77 ± 0.97	–	B19
“	–	−0.47 ± 0.16	D19 (**)
Ton 2	−184.4 ± 2.2	−0.70	H10
“	−172.7 ± 0.8	−0.26 ± 0.15	V18
“	−184.72 ± 1.12	–	B19
“	–	−0.26 ± 0.27	D19
“	−177.9 ± 4.0	−0.73 ± 0.03	G22

Notes. H10: Harris (2010), V18: Vásquez et al. (2018, in D16 scale), B19: Baumgardt et al. (2019), D19: Dias compilation, and G22: Geisler et al. (in prep.). (**)Taken from H10 with an offset (i.e., it is not a spectroscopic metallicity).

associate them with either an in situ or ex situ (accreted) origin, and often can also identify the latter with a particular accreted progenitor. A number of papers have carried out dynamical classifications of as many GCs as possible (e.g., Massari et al. 2019). Two of the most recent of these are Pérez-Villegas et al. (2020) and Callingham et al. (2022). Although *Gaia* is not as effective in deriving proper motions for heavily reddened crowded BGCs, excellent data still exists for almost all of them, allowing an almost definitive classification. What we have learned from this exercise is that most if not all halo GCs have been accreted and that there are indeed separate bulge and thick-disk GC populations that were both born in situ.

Looking at our sample of BGCs in Pérez-Villegas et al. (2020), we find that all but three are classified as bulge–bar clusters, while Terzan 12 and Ton 2 are deemed thick-disk clusters and Terzan 10 is denoted as an inner halo cluster. Callingham et al. (2022) make very similar classifications, with all of our sample being assigned to the bulge except BH 261, Terzan 10 and 12, and Ton 2, which are assigned to the Kraken progenitor. These classifications also agree very well with those of Massari et al. (2019), with the exception that NGC 6401 was also listed as a low-energy cluster, as was Ton 2, and Terzan 10 was associated with the *Gaia*-Enceladus-Sausage progenitor. We note that Terzan 10 is the lowest metallicity cluster in our sample as well, so that its extra-Bulge and extra-Galactic origin are not unexpected (see below). However, it is important to also note that our RV is 270 km s^{-1} different from that of B19, so that one must be careful to use the correct RV when deriving orbits. Ortolani et al. (2019) used a preliminary version of our value to calculate the Terzan 10 orbit, and find that it is clearly a halo intruder, currently only passing through the bulge. We caution that our RV is also very different from that of B19 for Terzan 9. Thus, most of our clusters are indeed BGCs, with the notable exceptions of the most metal-poor and two of the four most metal-rich.

We finally note that the census of Galactic GCs, especially BGCs, is probably still quite incomplete. Near-IR surveys like VVV/X have uncovered a large number of GC candidates in the bulge and adjacent disk in recent years (e.g., Minniti et al. 2010; Moni Bidin et al. 2011; Camargo & Minniti 2019; Palma et al. 2019; Garro et al. 2022) and some of these, on close inspection including the use of spectroscopy, turn out to indeed be previously unknown GCs (e.g., Dias et al. 2022a). However, not all of these candidates turn out to be true GCs (e.g., Gran et al. 2019; Minniti et al. 2021b; G21; G22) and care must be taken to use all weapons at our disposal (e.g., central concentration and density, field correction, dereddening, RV, proper motion, CMD, abundances, presence of RR Lyrae) to correctly identify the true nature of these candidates in this very difficult region.

7.2. The BGC metallicity distribution

Since the seminal work of Zinn (1985), it has been known that a key distinguishing characteristic of halo and bulge–disk GCs is their MD. He showed that halo GCs are mostly metal poor with a peak at [Fe/H] ∼ −1.6, whereas disk GCs are mostly metal rich, peaking around −0.5, with an intermediate minimum near −0.8. Of course, the quantity and especially quality of metallicities available some 40 years ago was limited and very crude compared to today’s standards, in particular for BGCs, yet the above basic impression of a unimodal metal-rich BGC system still persists. It is of some interest to revisit the BGC MD with modern data, including our own, and compare it with recent determinations of the bulge field star MD.

A relatively recent examination of BGCs was carried out by Bica et al. (2016), but they used the H10 metallicities, which are still not optimum, and defined BGCs only by R_{GC} and [Fe/H]. They found a bimodal MD for BGCs, with peaks around

−0.5 and −1.1. The metal-rich peak is the well-known classical Zinn (1985) peak, but they demonstrated that the metal-poor peak is perhaps dominant.

A more recent study is that of Pérez-Villegas et al. (2020), with metallicities taken from a wide variety of sources, but including their assessment of GC origin using *Gaia* DR2 proper motions. For their sample of 29 bona fide bulge–bar GCs, they uncovered the same two peaks as Bica et al. (2016), as well as a small group of only three GCs with even lower metallicities, ranging from −1.4 to −1.6. The reality of this possible low-metallicity peak in the MD of genuine BGCs is of course of interest, particularly since such clusters, if indeed BGCs, could well include the oldest in situ GC in the Galaxy. We note that their sample does not include the halo interloper Terzan 10 noted above. A more careful analysis including the best metallicities as well as the available RVs is needed to definitively assess this issue.

We plot our results in Fig. 10, where we compare our values to those from the Dias et al. catalog[2] for different GC classes. Our bona fide BGC sample is distributed over and between the two main BGC metallicity peaks. Our data does not strongly support a simple bimodal distribution with the above peak values, but clearly our sample is too small to draw any definitive conclusions. Again, better metallicities for the largest possible sample are required to clarify the nature of the BGC MD. Our halo GC and two disk GCs fall nicely within the MD of their class. We note again that our lowest metallicity cluster, Terzan 10, is now considered to be an inner halo cluster and not a BGC. Our most metal-poor bona fide BGC is BH 261 at [Fe/H] = −1.21.

Are there any true BGCs with metallicities lower than [Fe/H] ∼ −1.25? Our small sample does not contain any. However, the CAPOS study of G21 does find three such clusters, Terzan 4 and 9, and HP 1, with [Fe/H] from −1.2 to −1.4, all classified as bulge by Pérez-Villegas et al. (2020) and Callingham et al. (2022). As discussed above, CAPOS metallicities are substantially lower in the mean than our CaT values for the clusters in common, as is the case for Terzan 9. There is strong interest in determining reliable metallicities and ages for such metal-poor BGCs, in particular those with a blue horizontal branch, as they are excellent candidates for the oldest native GCs of the Milky Way (Lee et al. 1994; Barbuy et al. 2006, 2018b; Dias et al. 2016a), since they were born in situ. Even though these clusters are more metal rich than the peak of the halo MD, they could indeed be older than their lower metallicity halo couterparts given the expected more rapid chemical evolution in the deeper potential well of the proto-Galaxy as opposed to the shallower wells of much lower mass progenitors that generated the accreted halo GCs (Cescutti et al. 2008).

We also compared our BGC MD with that of bulge field stars. Probably the best recent bulge field star MD was derived by Rojas-Arriagada et al. (2020) from APOGEE spectra. They compiled a total of ∼13 000 bulge stars and find strong evidence for trimodality, with peaks at [Fe=H] = +0.32, −0.17, and −0.66. These peaks maintain their values, but their relative strengths vary as a function of Galactic latitude. The fraction of stars below −1 is very small, in contrast to our sample. It is likely that the most metal-poor field-star peak and metal-rich GC peak have similar origins. However, it is unclear why the field and GC MDs are otherwise quite distinct. One possible explanation could be the quite different age distributions (i.e., different formation epochs). Although GCs are all "old" (i.e., >10 Gyr or so) we do not have very accurate ages for the field stars, which could be somewhat younger, and thus more metal rich. We note that bulge RR Lyrae stars peak at around [Fe/H] = −1.0 (Dékány et al. 2013). Clearly, further improvement of both the quality and number of BGC metallicities is required to help address these puzzles.

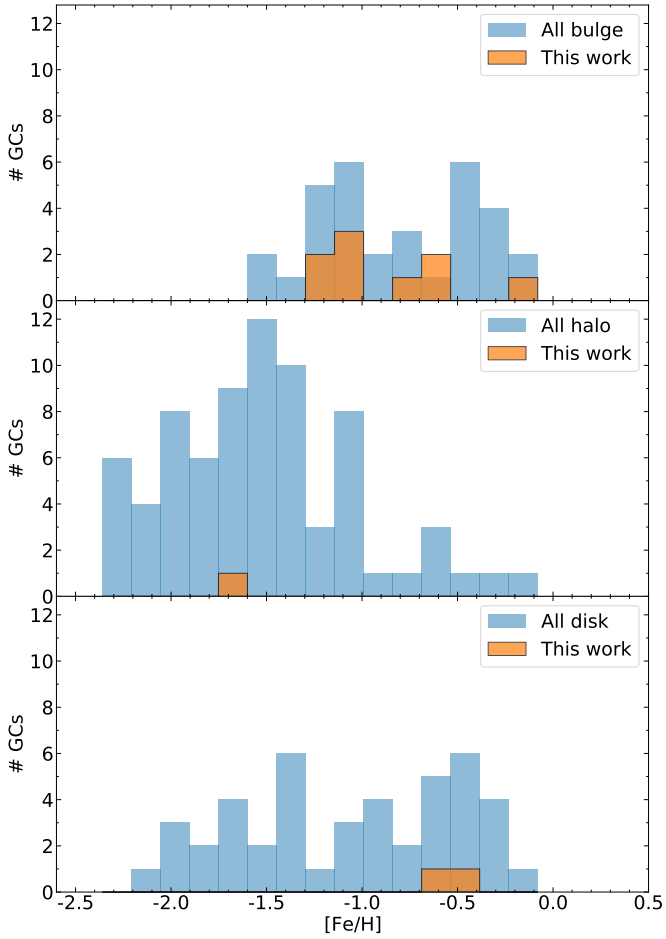

Fig. 10. Metallicity distribution function of all Galactic GCs from the metallicity scale of Dias et al. (2016a,b 2019 version[2]) shown as a blue histogram split by population following the same classification adopted in Fig. 1. The orange histogram represents the respective GC samples analyzed in this work adopting the metallicities derived here applying the V18 scale, as shown in Table 3.

8. Conclusions

We obtained low-resolution spectra of the CaT lines in a total of about 540 red giants in the vicinity of 13 bulge GCs using the FORS2 instrument on the Very Large Telescope. The targeted clusters were those that did not have spectra of individual stars at the time of our observations because of high reddening, and therefore had rather poor estimates of RVs and especially metallicities. We measured the wavelengths and equivalent widths of the CaT lines and derived RVs and metallicities using standard procedures. An extensive membership assessment involving the position in the cluster and CMD, RV, metallicity, and proper motion insured very high membership probabilities for our final sample. Unfortunately, we discovered that one of our clusters, VVV CL002, did not have any members among our observed stars. We derived mean cluster RV values with a mean standard error of the mean of 3 km s^{-1}, and mean metallicities to 0.05 dex for an average of 11 members per cluster for the remaining sample.

Next, we compared our mean RVs and metallicities with previous literature values for each cluster, focusing on determinations from five recent internally homogeneous catalogs. Overall agreement with the published RV values is generally good, but suggests our values are about 3 km s^{-1} lower on average. For [Fe/H], our mean values tend to agree with V18 and to a lesser extent with D19, which are on the same metallicity scale. Particularly puzzling is a mean offset of about 0.2 dex to higher metallicities for our results compared to the recent high-resolution study of G22.

We then discussed the nature of our GCs, finding that almost all of them are indeed bona fide BGCs. However, the most metal-poor cluster, Terzan 10, is likely a halo intruder, as first noted by Ortolani et al. (2019), while two of the most metal-rich are likely thick-disk GCs. Finally, we examine the MD of BGCs, comparing them to both halo and disk GCs, and to bulge disk stars. Our BGCs roughly follow the MD of other BGCs with metallicities on the same scale, including five clusters with [Fe/H] $\lesssim -1.0$. The possibility of a small, even more metal-poor group ([Fe/H] $\lesssim -1.25$) is currently unclear, and may only include further halo interlopers. The metal-rich peak coincides with the metal-poorest peak of the trimodal bulge field star distribution, leaving the more metal-poor BGCs with very few field star counterparts except for the RR Lyrae.

Acknowledgements. D.G. gratefully acknowledges support from the ANID BASAL project ACE210002. D.G. also acknowledges financial support from the Dirección de Investigación y Desarrollo de la Universidad de La Serena through the Programa de Incentivo a la Investigación de Académicos (PIA-DIDULS). S.V. and D.G. gratefully acknowledge the support provided by Fondecyt reg. 1220264. S.V. also acknowledges the the support provided by ANID BASAL projects ACE210002 and FB210003. This research was partially supported by the Argentinian institutions CONICET, SECYT (Universidad Nacional de Córdoba) and Agencia Nacional de Promoción Científica y Tecnológica (ANPCyT). B.D. acknowledges support by ANID-FONDECYT iniciación grant No. 11221366. D.M. gratefully acknowledges support by the ANID BASAL projects ACE210002 and FB210003 and by Fondecyt Project No. 1220724. We appreciate helpful comments raised by the referee. Based on observations collected at the European Southern Observatory under ESO programmes 089.D-0392 and 091.D-0389(A). This research has made use of the services of the ESO Science Archive Facility. This work has made use of data from the European Space Agency (ESA) mission *Gaia* (https://www.cosmos.esa.int/gaia), processed by the *Gaia* Data Processing and Analysis Consortium (DPAC, https://www.cosmos.esa.int/web/gaia/dpac/consortium). Funding for the DPAC has been provided by national institutions, in particular the institutions participating in the *Gaia* Multilateral Agreement.

References

Alonso-García, J., Dékány, I., Catelan, M., et al. 2015, AJ, 149, 99
Alonso-García, J., Smith, L. C., Catelan, M., et al. 2021, A&A, 651, A47
Appenzeller, I., Fricke, K., Fürtig, W., et al. 1998, The Messenger, 94, 1
Armandroff, T. E. 1989, AJ, 97, 375
Armandroff, T. E., & Da Costa, G. S. 1991, AJ, 101, 1329
Armandroff, T. E., & Zinn, R. 1988, AJ, 96, 92
Babusiaux, C., Gómez, A., Hill, V., et al. 2010, A&A, 519, A77
Barbuy, B. 2018, in The Galactic Bulge at the Crossroads, 54
Barbuy, B., Zoccali, M., Ortolani, S., et al. 2006, A&A, 449, 349
Barbuy, B., Zoccali, M., Ortolani, S., et al. 2009, A&A, 507, 405
Barbuy, B., Chiappini, C., & Gerhard, O. 2018a, ARA&A, 56, 223
Barbuy, B., Muniz, L., Ortolani, S., et al. 2018b, A&A, 619, A178
Baumgardt, H., & Hilker, M. 2018, MNRAS, 478, 1520
Baumgardt, H., Hilker, M., Sollima, A., & Bellini, A. 2019, MNRAS, 482, 5138
Bica, E., Ortolani, S., & Barbuy, B. 2016, PASA, 33
Bovy, J., Leung, H. W., Hunt, J. A. S., et al. 2019, MNRAS, 490, 4740
Bressan, A., Marigo, P., Girardi, L., et al. 2012, MNRAS, 427, 127
Callingham, T. M., Cautun, M., Deason, A. J., et al. 2022, MNRAS, 513, 4107
Camargo, D., & Minniti, D. 2019, MNRAS, 484, L90
Carretta, E., Bragaglia, A., Gratton, R., D'Orazi, V., & Lucatello, S. 2009, A&A, 508, 695
Cescutti, G., Matteucci, F., Lanfranchi, G. A., et al. 2008, A&A, 491, 401
Cohen, R. E., Mauro, F., Alonso-García, J., et al. 2018, AJ, 156, 41
Cohen, R. E., Bellini, A., Casagrande, L., et al. 2021, AJ, 162, 228
Cole, A. A., Smecker-Hane, T. A., Tolstoy, E., Bosler, T. L., & Gallagher, J. S. 2004, MNRAS, 347, 367
Côté, P. 1999, AJ, 118, 406
Dékány, I., Minniti, D., Catelan, M., et al. 2013, ApJ, 776, L19
Dias, B., & Parisi, M. C. 2020, A&A, 642, A197
Dias, B., Barbuy, B., Saviane, I., et al. 2016a, A&A, 590, A9
Dias, B., Saviane, I., Barbuy, B., et al. 2016b, The Messenger, 165, 19
Dias, B., Angelo, M. S., Oliveira, R. A. P., et al. 2021, A&A, 647, L9
Dias, B., Parisi, M. C., Angelo, M., et al. 2022a, MNRAS, 512, 4334
Dias, B., Palma, T., Minniti, D., et al. 2022b, A&A, 657, A67
Ernandes, H., Dias, B., Barbuy, B., et al. 2019, A&A, 632, A103
Fernández-Trincado, J. G., Beers, T. C., Minniti, D., et al. 2020, A&A, 643, L4
Fernández-Trincado, J. G., Minniti, D., Souza, S. O., et al. 2021, ApJ, 908, L42
Fernández-Trincado, J. G., Villanova, S., Geisler, D., et al. 2022, A&A, 658, A116
Gaia Collaboration (Luri, X., et al.) 2021, A&A, 649, A7
Garro, E. R., Minniti, D., Alessi, B., et al. 2022, A&A, 659, A155
Geisler, D., Villanova, S., O'Connell, J. E., et al. 2021, A&A, 652, A157
Girardi, L., & Salaris, M. 2001, MNRAS, 323, 109
Gonzalez, O. A., & Gadotti, D. 2016, in Galactic Bulges, Astrophys. Space Sci. Lib., 418, 199
Gran, F., Zoccali, M., Contreras Ramos, R., et al. 2019, A&A, 628, A45
Harris, W. E. 1996, AJ, 112, 1487
Harris, W. E. 2001, in Saas-Fee Advanced Course 28: Star Clusters, eds. L. Labhardt, & B. Binggeli, 223
Harris, W. E. 2010, arXiv e-prints [arXiv:1012.3224]
Husser, T.-O., Latour, M., Brinchmann, J., et al. 2020, A&A, 635, A114
Idiart, T. P., Barbuy, B., Perrin, M. N., et al. 2002, A&A, 381, 472
Kerber, L. O., Libralato, M., Souza, S. O., et al. 2019, MNRAS, 484, 5530
King, I. R. 1966, AJ, 71, 64
Kunder, A., Rich, R. M., Koch, A., et al. 2016, ApJ, 821, L25
Lee, Y.-W., Demarque, P., & Zinn, R. 1994, ApJ, 423, 248
Majewski, S. R., Schiavon, R. P., Frinchaboy, P. M., et al. 2017, AJ, 154, 94
Massari, D., Koppelman, H. H., & Helmi, A. 2019, A&A, 630, L4
Mauro, F., Moni Bidin, C., Geisler, D., et al. 2014, A&A, 563, A76
Minniti, D. 1995, AJ, 109, 1663
Minniti, D., Lucas, P. W., Emerson, J. P., et al. 2010, Nat. Astron., 15, 433
Minniti, D., Hempel, M., Toledo, I., et al. 2011, A&A, 527, A81
Minniti, D., Fernández-Trincado, J. G., Smith, L. C., et al. 2021a, A&A, 648, A86
Minniti, D., Palma, T., & Clariá, J. J. 2021b, Boletin de la Asociacion Argentina de Astronomia La Plata Argentina, 62, 107
Moni Bidin, C., Mauro, F., Geisler, D., et al. 2011, A&A, 535, A33
Nidever, D. L., Hasselquist, S., Hayes, C. R., et al. 2020, ApJ, 895, 88
Olszewski, E. W., Schommer, R. A., Suntzeff, N. B., & Harris, H. C. 1991, AJ, 101, 515
Ortolani, S., Barbuy, B., Bica, E., et al. 1999, A&A, 350, 840
Ortolani, S., Nardiello, D., Pérez-Villegas, A., Bica, E., & Barbuy, B. 2019, A&A, 622, A94
Palma, T., Minniti, D., Alonso-García, J., et al. 2019, MNRAS, 487, 3140
Parisi, M. C., Grocholski, A. J., Geisler, D., Sarajedini, A., & Clariá, J. J. 2009, AJ, 138, 517
Parisi, M. C., Geisler, D., Clariá, J. J., et al. 2015, AJ, 149, 154
Parisi, M. C., Geisler, D., Carraro, G., et al. 2016, AJ, 152, 58
Parisi, M. C., Gramajo, L. V., Geisler, D., et al. 2022, A&A, 662, A75
Pérez-Villegas, A., Barbuy, B., Kerber, L. O., et al. 2020, MNRAS, 491, 3251
Pietrukowicz, P., Kozłowski, S., Skowron, J., et al. 2015, ApJ, 811, 113
Rojas-Arriagada, A., Zasowski, G., Schultheis, M., et al. 2020, MNRAS, 499, 1037
Rossi, L. J., Ortolani, S., Barbuy, B., Bica, E., & Bonfanti, A. 2015, MNRAS, 450, 3270
Rutledge, G. A., Hesser, J. E., Stetson, P. B., et al. 1997, PASP, 109, 883
Saviane, I., Da Costa, G. S., Held, E. V., et al. 2012, A&A, 540, A27
Saviane, I., Zoccali, M., Minniti, D., Geisler, D., & Dias, B. 2020, The Messenger, 179, 31
Shapley, H. 1918, PASP, 30, 42
Valenti, E., Ferraro, F. R., & Origlia, L. 2007, AJ, 133, 1287
Valenti, E., Ferraro, F. R., & Origlia, L. 2010, MNRAS, 402, 1729
Valenti, E., Origlia, L., Mucciarelli, A., & Rich, R. M. 2015, A&A, 574, A80
Vasiliev, E., & Baumgardt, H. 2021, MNRAS, 505, 5978
Vásquez, S., Zoccali, M., Hill, V., et al. 2015, A&A, 580, A121
Vásquez, S., Saviane, I., Held, E. V., et al. 2018, A&A, 619, A13
Zinn, R. 1985, ApJ, 293, 424
Zinn, R., & West, M. J. 1984, ApJS, 55, 45
Zoccali, M., & Valenti, E. 2016, PASA, 33
Zoccali, M., Vasquez, S., Gonzalez, O. A., et al. 2017, A&A, 599, A12